

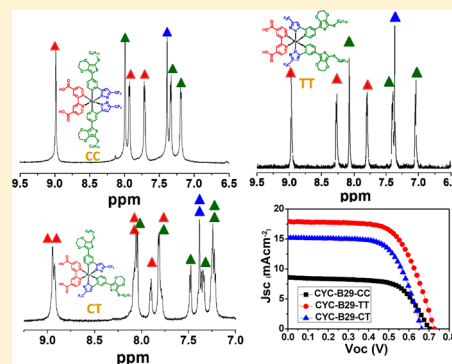
Diastereoisomers of Ruthenium Dyes with Unsymmetric Ligands for DSC: Fundamental Chemistry and Photovoltaic Performance

Jheng-Ying Li,[‡] Chia Lee,[†] Chia-Yuan Chen,^{†,‡} Wen-Long Lee,[†] Ren Ma,[†] and Chun-Guey Wu^{*,†,‡}

[†]Department of Chemistry and [‡]Research Center for New Generation Photovoltaics, National Central University, Jhong-Li 32001, Taiwan, ROC

Supporting Information

ABSTRACT: A new thiocyanic acid-free ruthenium sensitizer, CYC-B29, containing two unsymmetrical ancillary ligands, was synthesized, and its three diastereoisomers CYC-B29-CC, CYC-B29-TT, and CYC-B29-CT with significantly different optical, electronic, and electrochemical properties were carefully separated. CYC-B29-TT with the smallest size has the strongest absorption coefficient of the MLCT band, the shortest λ_{max} , the lowest highest occupied molecular orbital level and the highest dye loading. Therefore, dye-sensitized solar cell based on CYC-B29-TT has the highest efficiency, which is two times higher than that of CYC-B29-CC-sensitized device and 10% higher than that of N719-based cell. Time-dependent density functional theory-calculated transition bands for the three isomers are not identical, and only CYC-B29-TT has the calculated transition bands close to the experimental absorption profile. Although the calculated transition bands for CYC-B29-CC and CYC-B29-CT are not consistent with the experimental data, the ground-state vertical excitation energy with oscillator strength and electron-density difference map data combining with the dye loading predict correctly the order of the photocurrent for the three isomers sensitized devices.



INTRODUCTION

Dye-sensitized solar cell (DSC) showed great promise for the future renewable energy due to its possible low manufacture cost and diverse materials available for every component in DSC.^{1–3} Dye molecule (sensitizer), which absorbs photon and produces movable electron, plays a vital role in the light harvesting, charge separation, and the overall power conversion efficiency (PCE) of the devices. Thousands of dye molecules were scrutinized, and ruthenium complexes have been proved to be one of the most effective sensitizers to be used in DSC. The high photovoltaic performance (i.e., efficiency > 11%) ruthenium-based dyes (such as N719,⁴ CYC-B11,⁵ and C106⁶) were all derived from N3 ([Ru(dcbpy)₂(NCS)₂]; dcbpy = 4,4'-dicarboxy-2,2'-bipyridine) dye,⁷ which contains two thiocyanate (NCS⁻) ligands. Despite their excellent efficiency, thiocyanate is a monodentate ligand, which may be unstable under excessive thermal stress and/or light soaking.^{8,9} This disadvantage has triggered the research for the effective chelating ligands to replace thiocyanate in ruthenium-based sensitizers.^{10–17}

A first successful example for using NCS-free ruthenium sensitizer in DSC to achieve high (10.1%) efficiency was reported by Grätzel et al., who used a bidentated 2,4-difluorophenylpyridinato to replace two NCS to prepare a cyclometalated tris-bidentate ruthenium complex, YE05.¹⁸ Subsequent studies on using cyclometalating chelates^{19–24} and other multidentate ligands^{25,26} to prepare NCS-free Ru(II) complexes for DSC applications were reported by several research groups, and Chi et al. is one of the representative

groups. They used one 4,4'-carboxy-2,2'-bipyridine and two 2-pyridyl pyrazolate ligands to synthesize a series of neutral, thiocyanate-free Ru(II) sensitizers (TFRS-x). DSC based on TFRS-2 has the efficiency of 9.54% (vs 8.56% for N719-sensitized device).¹⁹ They also used 2-pyridyl triazolate²⁷ or isoquinolinyl pyrazolate²⁸ to prepare a series of NCS-free heteroleptic tris-bidentate cyclometalated ruthenium sensitizers and demonstrated that all these NCS-free ruthenium sensitizers have good photovoltaic performance and long-term stability.^{19–28}

Most bidentate ancillary ligands used in NCS-free ruthenium complexes have an unsymmetrical structure, and the resulting complex has three diastereoisomers. These three diastereoisomers (not easy to be separated) may have different physicochemical properties and photovoltaic performance. A paper, published by Chi²⁹ et al. last year, has studied the photovoltaic performance of two old dyes containing unsymmetrical ancillary ligand. They isolated only two diastereoisomers (of the three) and found that the physicochemical properties of the two diastereoisomers are very similar. Therefore, the variation in the photovoltaic performance of the two isomers is mainly due to the different surface coverage of the mesoporous TiO₂ film, which was determined by the molecular conformation of the isomers. We are developing high-efficiency NCS-free ruthenium dyes for DSC and find that the efficiency of the device is affected apparently by the purity

Received: August 28, 2015

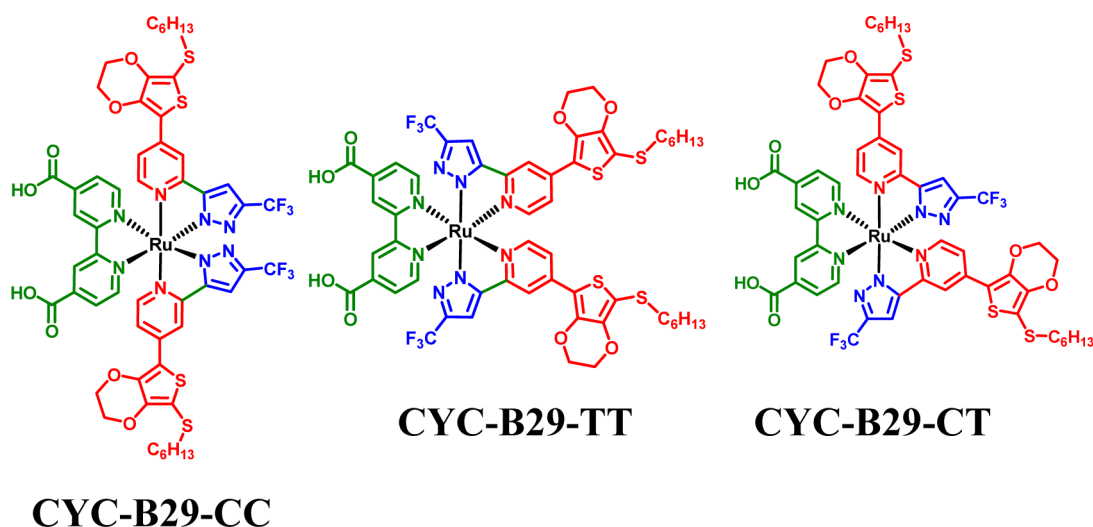


Figure 1. Structure of the three diastereoisomers: CYC-B29-CC, CYC-B29-TT, and CYC-B29-CT.

of the isomers. Therefore, the physicochemical properties of the three diastereoisomers may not be the same. To really understand the fundamental chemistry and photophysics of the diastereoisomers, a new NCS-free ruthenium sensitizer (code CYC-B29) with unsymmetrical ancillary ligands was prepared. The three diastereoisomers (CYC-B29-CC, CYC-B29-TT, and CYC-B29-CT) were carefully separated, and their photovoltaic performance was investigated. The three diastereoisomers are different not only in the photovoltaic performance but also in the optical, electronic, and electrochemical properties.

RESULTS AND DISCUSSION

The structures of the three diastereoisomers of 4-(5-thiohexyl-(3,4-ethylene-dioxythiophen-2-yl))-2-(3-(trifluoromethyl)-1*H*-pyrazol-5-yl)pyridine (CYC-B29) are displayed in **Figure 1**: their names (CYC-B29-CC, CYC-B29-TT, and CYC-B29-CT) were defined by the pyridine unit in the ancillary ligand, considering if it is trans or cis to the pyridine ring of the anchoring ligand. The detailed two-step synthetic procedure, isolation, and identification of the three isomers can be found in the electronic **Supporting Information**. The ^1H NMR spectra of the three isomers are displayed in **Figure S1**, and the peak assignment is based on the paper reported by Chi¹⁹ et al. The yields of CYC-B29-CC, CYC-B29-TT, and CYC-B29-CT are 8%, 17%, and 10%, respectively. CYC-B29-CC and CYC-B29-CT isomers have a similar yield; nevertheless, the yield of CYC-B29-TT, which has the two pyrazole (Paz) units trans to each other, is almost two times of that for the other two isomers. This may be because the trans effect of Paz is higher than that of pyridine, which means the ligand trans to Paz is less stable compared to that trans to pyridine. Therefore, two Paz units trans to each other (in TT isomer) are more stable compared to those (CC and CT isomers) with two Paz units cis to each other. We prepared several batches of CYC-B29 dye, and the ratios of the yields for the three isomers are very close: TT isomer has the yield always approximately two times of the other two isomers.

The electronic absorption spectra of the three diastereoisomers measured in dimethylformamide (DMF) and immobilized on the transparent TiO_2 film (thickness is ca. 3 μm) are displayed in **Figure 2**, and the optical data were summarized in Table S1, **Supporting Information**. The three

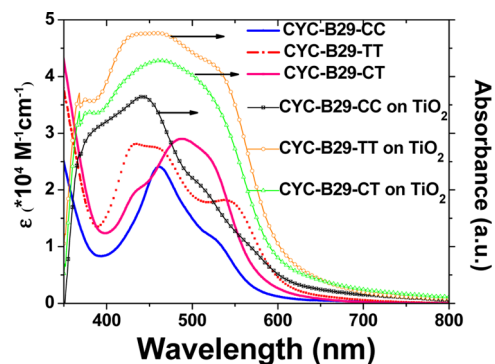


Figure 2. Absorption spectra of the three diastereoisomers measured in DMF and immobilized on the transparent TiO_2 film (thickness is ca. 3 μm).

diastereoisomers in DMF have significantly different absorption profiles: CYC-B29-CC has a strong absorption peak at 462 nm with a shoulder at longer wavelength, CYC-B29-CT has λ_{max} at 489 nm with a shoulder at each side of the peak, whereas CYC-B29-TT has two defined peaks centered at 434 and 540 nm, respectively; all these bands may relate to the metal-to-ligand charge transfer (MLCT) bands. Furthermore, the absorption intensity at the visible region (the integration of the absorption coefficient between 350 and 750 nm) for the three isomers is also different: CYC-B29-TT and CYC-B29-CT have similar integrated visible light absorption intensity, while the integrated absorption intensity of CYC-B29-CC is much lower than the other two isomers. The possible reason for the low light harvesting ability of CYC-B29-CC isomer will be discussed more in later paragraphs.

All isomers are blue-shifted when adsorbed on TiO_2 thin film, indicating that CYC-B29 undergoes a H-aggregation or a conformational change induced by the deprotonation in the self-assembly process. The absorption spectra of the specific dyes varied when adsorbed on TiO_2 anode. For example the absorption profiles for CYC-B29-TT and CYC-B29-CT adsorbed TiO_2 films are similar, even though their absorption profiles are different in DMF. On the contrary, the absorption profiles of CYC-B29-CC and CYC-B29-TT in DMF are similar, but they differ after adsorption on TiO_2 film. Nevertheless, the absorption of CYC-B29-CC adsorbed on TiO_2 film is much

weaker (especially at long wavelength, which correlated to MLCT band) compared to those of the other two isomers adsorbed on TiO_2 , consistent with the smallest absorption coefficient of CYC-B29-CC dye. The significant variation in the absorption profile for the dye dissolved in DMF and adsorbed on TiO_2 was not observed in the high-performance ruthenium dye with two NCS ligands we prepared.^{5,30,31} Interestingly, for the dyes adsorbed on a TiO_2 film, the absorption onset extends to longer wavelength for all three isomers. The widening in absorption profile is reasonably attributed to dye molecules with various conformations coexisting on TiO_2 surface, due to the bulky nature of NCS-free ruthenium complexes. Furthermore, the absorption intensity (in the visible region) of CYC-B29-TT is close to that of CYC-B29-CT in DMF, but CYC-B29-TT-sensitized TiO_2 thin film has stronger absorption than CYC-B29-CT-sensitized TiO_2 . This is due to CYC-B29-TT with symmetric slender conformation occupying less space when adsorbed on TiO_2 compared to CYC-B29-CT, which has an unsymmetrical more spherical-like conformation.

The graphical representation of the computed frontier orbitals for the three isomers is displayed in Figures S2–S4. The distribution of the frontier orbitals for the three isomers is similar: highest occupied molecular orbital (HOMO), HOMO–1, and HOMO–2 are mainly located on the metal center and Paz units, while HOMO–3 and HOMO–4 are contributed primarily from the ethylene–dioxythiophene (EDOT)–pyridine moiety of the ancillary ligand. However, the lowest unoccupied molecular orbital (LUMO), LUMO+1, and LUMO+4 locate on the anchoring ligand, while LUMO+2 and LUMO+3 mainly distribute on the ancillary ligands. Nevertheless, since the relative position of the two Paz units is different, the contour of the electron density map of the frontier orbitals is quite different in three isomers, even though the orbitals are contributed by the same chemical identity. For example the HOMO of both CC and TT isomers is mainly contributed from Ru center and two Paz units. However, the conformation of two Paz units in CC is bending, whereas that for TT is linear. Similar situations happened in LUMO+2 and LUMO+3 orbitals, which distribute predominantly on EDOT units of the ancillary ligands. The significant difference in the absorption spectra for the three diastereoisomers should be attributed to the difference in the contour of the electron density map of the frontier orbitals. Nevertheless, the subtle different contour of the electron density map cannot be used to explain the significant difference in the absorption profile of the three diastereoisomers.

To gain more insight into the absorption bands, time-dependent density functional theory (TD-DFT) calculation of the singlet electronic transition was performed with DMF as the solvent. The calculated absorption peaks and electron density difference maps (EDDMs) as well as the experimental absorption spectra for the three isomers are displayed in Figure 3, and the detailed transition assignments are listed in Tables S2–S4. The computed singlet transitions for the three isomers have no big difference. All isomers have a moderate transition at 535–545 nm, belong to H-2→L transition, and several peaks occur at 400–460 nm although the relative intensity of the peaks for the three isomers is not the same. However, only CYC-B29-TT has the calculation result that agreed well with the experimental spectrum, considering the energy and relative intensity of the peaks. The results reveal the limitation of the theoretical calculations when it was used to calculate the difference in the optical property of the diastereoisomers. CYC-

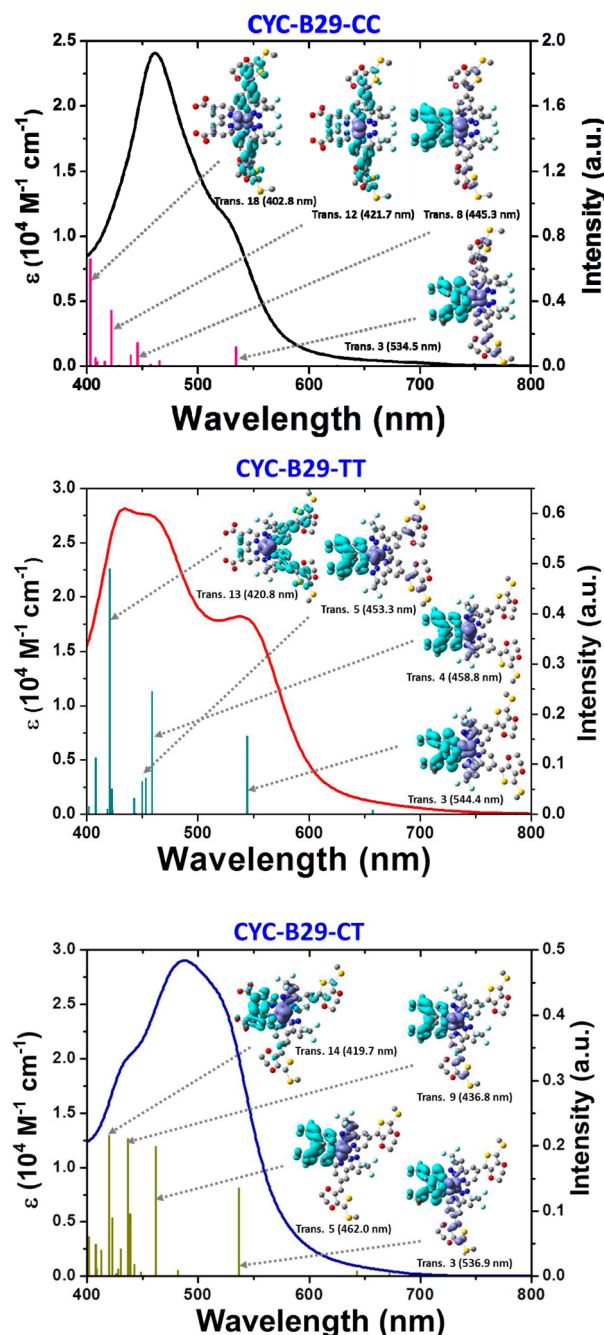


Figure 3. Calculated (DT-DFT) absorption peaks and EDDMs as well as the experimental absorption spectra for the three diastereoisomers of CYC-B29.

B29-TT has four strongest transitions occur at 544.4 nm (S_3 with oscillator strength $f = 0.1558$), 458.8 nm (S_4 with $f = 0.2446$), 453.3 nm (S_5 with $f = 0.0725$), and 420.8 nm (S_{13} with $f = 0.4901$). Three of them (except that at 420.8 nm) with total oscillator strength of 0.4729 are attributed to the beneficial (MLCT) charge transfer from Ru orbitals (or Ru-Paz mixed orbitals) to the anchoring ligand. These transitions are believed to be contributing significantly to the photo absorption, electron injection, and photocurrent production. Nevertheless, the calculated and experimental spectra for CYC-B29-CC are not the same. Peaks for the four strongest calculated absorptions are 534.5 nm (S_3 with oscillator strength $f = 0.1231$), 445.3 nm (S_8 with $f = 0.1442$), 421.7 nm (S_{12} with $f =$

0.3437), and 402.8 nm (S_{18} with $f = 0.6623$). Only two of the four peaks with total oscillator strength of 0.2673 are strongly related to the metal-to-anchoring ligand charge transfer. The calculated absorption bands are also not quite consistent with the experimental absorption spectrum for CYC-B29-CT. The four strongest calculated absorptions are 536.9 nm (S_3 with oscillator strength (f) = 0.1350), 462.0 nm (S_5 with $f = 0.1987$), 436.8 nm (S_9 with $f = 0.2114$), and 419.7 nm (S_{14} with $f = 0.2162$), and three of the four transitions (total oscillator strength is 0.5451) are mainly contributed from Ru-Paz to the bipyridine ring (not the COOH) of the anchoring ligand charge transfer. Therefore, the excited electron (from the absorption at 419.7 nm) may linger at the bipyridine unit, cannot inject to TiO_2 through COOH anchoring moiety. On the basis of only the optical data (both theoretic and experimental) without considering the dye loading, we may expect that CYC-B29-CT-based DSC has the highest Jsc value, and the Jsc of the cell sensitized with CYC-B29-CC is the lowest.

The driving force for electron injection from the photo-excited dye into the conduction band of TiO_2 and the regeneration of oxidized dye by the electron from the redox couple depends on the energy level of the frontier orbitals of the dye molecule. The HOMO and LUMO energy levels of the three isomers determined by the square-wave voltammograms and the absorption thresholds are displayed in Figure 4. The

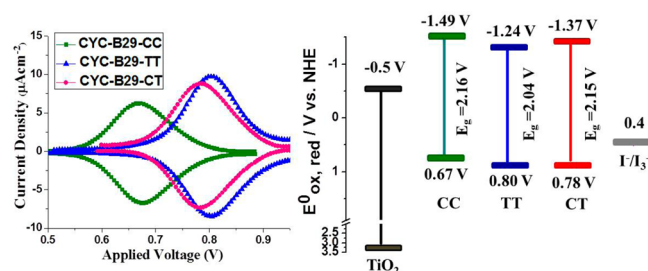


Figure 4. Voltammograms and energy level of the frontier orbitals for the three diastereoisomers of CYC-B29.

ground-state potentials of CYC-B29-CC, CYC-B29-TT, and CYC-B29-CT dissolved in DMF are 0.67, 0.80, and 0.78 V versus normal hydrogen electrode (NHE), respectively. The HOMOs of the three isomers are all higher than those for the complexes with NCS ligands we reported before^{5,30,31} but still more positive than the redox potential (~ 0.4 V vs NHE) of the iodide/triiodide electrolyte used in this study. The optical transition energy, E_{0-0} , determined from its absorption onset energy E_g measured in DMF is 2.16, 2.04, and 2.15 eV for CYC-B29-CC, CYC-B29-TT, and CYC-B29-CT, respectively. Therefore, the LUMO energy levels (LUMO = HOMO – E_g) for the three isomers are all much more negative than the conduction band of TiO_2 (ca. -0.5 V vs NHE),⁵² benefiting the electron injection from the excited dyes to TiO_2 anode. Nevertheless, the HOMO of CYC-B29-CC is only 0.27 V lower than the redox potential of iodide electrolyte. The energy difference may not provide sufficient driving force for the dye to be regenerated by iodide ion, which may result in low short-circuit current of the corresponding device.

The current–voltage (I – V ; measured under the illumination of AM 1.5G simulated sunlight (100 mW cm^{-2}) and incident photon-to-current conversion efficiency (IPCE) curves for CYC-B29 sensitized devices are shown in Figure 5, and the

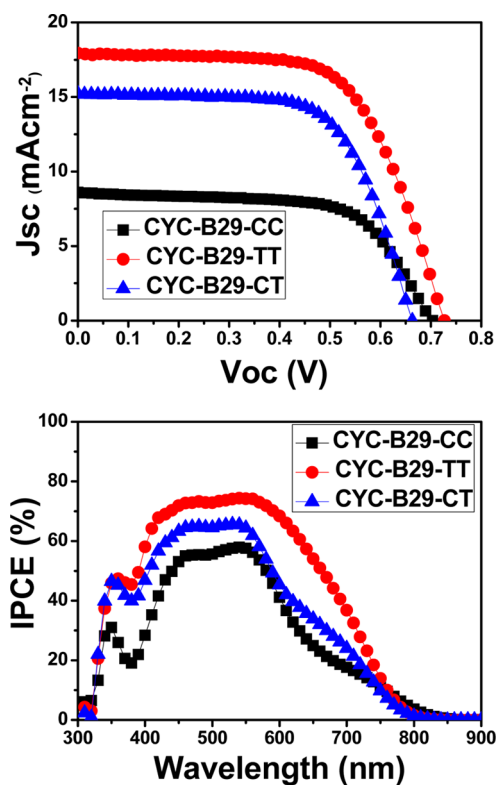


Figure 5. I – V and IPCE curves of CYC-B29 sensitized devices.

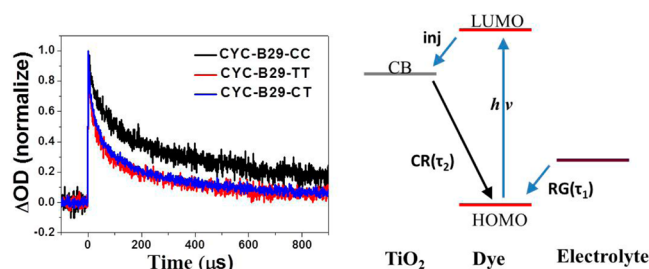
photovoltaic parameters as well as the dye loading are summarized in Table 1. The IPCE spectra of the devices sensitized with the three isomers all show a broad spectral response in the range from 350 to 800 nm, reaching a maximum value of 58%, 76%, and 66% for Device A (CYC-B29-CC-sensitized cell), Device B (CYC-B29-TT-sensitized cell), and Device C (CYC-B29-CT-sensitized cell), respectively. The IPCE value of the Device B is higher than those of the Device A and Device C at the whole measured wavelength, consistent with the absorption data of the dye-adsorbed TiO_2 thin film shown in Figure 2. Moreover, the dye loading for CYC-B29-TT is higher than that of the other two isomers (see Table 1). As shown in Figure 1 and Figure 3, the conformation of CYC-B29-TT molecule with the two longer axes parallel to the anchoring ligand occupies less TiO_2 surface compared to CYC-B29-CC or CYC-B29-CT isomers, which has two longer axes perpendicular to the anchoring ligand or one perpendicular, one parallel to the anchoring ligand. The absorption (dye loading \times absorption coefficient) of CYC-B29-TT is the strongest among the three diastereoisomers. That is why the Jsc of the Device B is higher than that for the Device C (based on CYC-B29-CT) although the effective MLCT band for CYC-B29-CT is stronger. Furthermore, CYC-B29-TT also has the HOMO energy level slightly lower than that of CYC-B29-CT (see Figure 4); therefore, it will have higher driven force for the regeneration of the oxidized dye by the electrolyte. This may also be one of the reasons that Device B has higher Jsc compared to Device C. Jsc for the Device A listed in Table 1 is much smaller than that of Device B. It is because CYC-B29-CC has smaller absorption coefficient, less dye loading, and weaker effective MLCT transition (from DT-DFT calculation) compared to CYC-B29-TT. Similar reasons (low absorption coefficient and weak effective metal-to-ligand charge transfer) also explain why the dye loading of CYC-B29-CC-sensitized

Table 1. Photovoltaic Parameters and TiO₂/Dye/Electrolyte Interphase Resistance (R_2) of the Cells Sensitized with the Three Diastereoisomers

dye	device	J _{sc} (mAcm ⁻²)	V _{oc} (V)	FF	η (%)	dye loading (mole)	R_2 (Ω)
CYC-B29-CC	A	8.61	0.704	0.643	3.90	2.8×10^{-8}	128
CYC-B29-TT	B	17.94	0.727	0.640	8.34	3.2×10^{-8}	578
CYC-B29-CT	C	15.23	0.663	0.659	6.66	2.3×10^{-8}	81.5
N719	R	14.42	0.772	0.680	7.55		

TiO₂ is close to that of CYC-B29-CT dyed anode but the J_{sc} of the Device A is significantly smaller than that of Device C.

J_{sc} of a cell is also affected by the kinetics of the dye regeneration, which was influenced by the HOMO level of the dye molecules. To probe the kinetics of dye regeneration, transient absorption spectra (TAS, Figure 6) of the devices

**Figure 6.** Transient absorption spectra of CYC-B29 sensitized devices.

were performed, and the calculated dye regeneration lifetimes (τ_1 and τ_2 corresponding to the reduction of the oxidized dye by I⁻ in electrolyte and by the electrons in TiO₂, respectively)⁵ as well as the amplitude ratios of the two reduction processes (A_1/A_2 ; can be regarded as the ratio of the oxidized dye reduced by electrolyte and electron in TiO₂) are summarized in Table 2. The driving forces (E_{D1} and E_{D2}) for the dye

Table 2. Dye Regeneration Driving Force, Lifetime and the Amplitude Ratio of the Two Dye Regeneration Paths

dye	^a E_{D1} (V vs NHE)	τ_1 (μ s)	^b E_{D2} (V vs NHE)	τ_2 (μ s)	amplitude ratio of τ_1 and τ_2 (A_1/A_2)
CYCB29- CC	0.27	58.42	1.17	818.97	48/52
CYCB29- TT	0.40	30.35	1.30	436.80	63/37
CYCB29- CT	0.38	38.84	1.28	499.29	64/36

$${}^a E_{D1} = (E_{\text{HOMO}} - E_{\text{redox of electrolyte}}) \quad {}^b E_{D2} = (E_{\text{TiO}_2 \text{ CB}} - E_{\text{HOMO}})$$

regeneration from two different paths are also listed in Table 2. The lifetime for the dye regenerated by electrolyte or electron in TiO₂ is inversely proportional to the driving force: the higher the driving force, the shorter the lifetime. Device A has the longest τ_1 indicating that the reducing of the oxidized dye by iodide in the electrolyte is slower than the other two isomers, due to the higher HOMO energy level of CYC-B29-CC, and therefore the oxidized dye will be reduced in more negative potential. The driving force (E_{D1}) for the dye regeneration of CYC-B29-CC is also smaller than that for the other two isomers. Device A also has the longest τ_2 value suggesting the back electron transfer from TiO₂ to the oxidized dye is not as serious as that for Device B and C, because it has the smallest driving force (E_{D2}). However, the amplitude ratio (A_1/A_2) for

the Device A listed in Table 2 is the smallest, suggesting that the ineffective reducing of the oxidized dye by iodide is the major reason for the poor photovoltaic performance of Device A. TAS data can also explain why the cell sensitized by CYC-B29-CC exhibits such low photocurrent density.

Data listed in Table 1 also reveal that CYC-B29-TT-sensitized device also has the highest Voc. It is known that the theoretical Voc of a DSC is defined by the potential difference between the quasi-Fermi level of TiO₂ and the redox potential of the electrolyte. Therefore, Voc was determined by the energy level of TiO₂ conduction band edge³³ and the degree of the electron recombination (from TiO₂ to the oxidized dye or electrolyte) of the cell.^{32,34} The former depends on the number of the electrons injected from the excited dye molecules to TiO₂, and the latter relies on the surface protection of TiO₂ anode. CYC-B29-TT has the largest dye loading and the largest absorption coefficient, the Fermi level of TiO₂ sensitized with CYC-B29-TT should be the highest, results in high Voc. The degree of the charge recombination (TiO₂ surface protection) for a DSC is influenced not only by the amount of adsorbed dye molecules but also on the conformation and size of the sensitizer. The information on the surface protection of TiO₂ anode can be obtained from the electrochemical impedance studies of the device under dark. The TiO₂/dye/electrolyte interphase resistances (R_2 , derived from the electrochemical impedance spectroscopy (EIS) diagrams illustrated in Figure S5) listed in Table 1 clearly reveal that TiO₂/dye/electrolyte interphase resistance of CYC-B29-TT sensitized device (Device B) is much larger than those for the other two devices (Device A and Device C) based on CYC-B29-CC and CYC-B29-CT isomers. Less charge recombination for the Device B would also be the reason for the higher Voc. As a result CYC-B29-TT-sensitized cell has the highest overall efficiency of 8.34%, which is ca. 10% higher than that of the Device R based on N719 dye fabricated at the same condition (see Table 1).

CONCLUSIONS

In summary, three diastereoisomers of a new NCS-free ruthenium sensitizer, CYC-B29, were carefully isolated. These isomers (CYC-B29-CC, CYC-B29-TT, and CYC-B29-CT) have significant variation in the molecular conformation and electronic, electrochemical, and photophysical properties and therefore have tremendously different photovoltaic performance when applied in DSC. CYC-B29-CC isomer has the lowest absorption coefficient, the smallest dye loading, and the highest HOMO energy level. Device A sensitized with CYC-B29-CC has the lowest J_{sc} and PCE. CYC-B29-CT has a similar dye loading (compared to CYC-B29-CC), but the corresponding cell has lower Voc, due to the poorer surface protection of the dyed TiO₂ since it has less bulky structure. However, the efficiency of the Device C (based on CYC-B29-CT) is still higher than that for Device A, because CYC-B29-CT has higher absorption coefficient and therefore higher J_{sc} of the corresponding cell. CYC-B29-TT (with a less-open

structure (slender conformation)) therefore has the highest dye-loading, the lowest HOMO energy level, and the largest absorption coefficient, the corresponding device (Device B) has the highest efficiency, which is two times higher than that of CYC-B29-CC-sensitized cell. Furthermore, only CYC-B29-TT isomer has the TD-DFT calculated transition bands close to the experimental absorption spectrum, implying that the electronic properties of the diastereoisomers may not be predicted precisely simply by routine theoretical calculation. Nevertheless, the calculated ground-state vertical excitation energy with oscillator strength and EDDM of the isomers afford the useful information for understanding the origin of the J_{sc} when applied in DSCs. This study provides not only the understanding of the basic chemistry of inorganic diastereoisomers but also the strategy for designing high-efficiency ruthenium dye for DSC.

EXPERIMENTAL SECTION

Materials, Synthesis, and Characterization. All reagents were obtained from the commercial sources and used as received unless specified. Solvents were dried over sodium or CaH_2 before use. The ancillary ligand B29 (4-(5-thiohexyl-(3,4-ethylene-dioxy-thiophen-2-yl))-2-(3-(trifluoromethyl)-1H-pyrazol-5-yl)pyridine) for CYC-B29 was prepared according to the literature report,¹⁹ and CYC-B29 dye was synthesized using two-step synthetic procedure. The detailed preparation procedures, as well as the characterization of the ancillary ligand and the final ruthenium complexes, can be found in the electronic Supporting Information. The structure of CYC-B29 dye was identified with 1H NMR spectrum, FAB-MS, and elemental analysis. The structure of the diastereoisomers was mainly assigned according to the paper¹⁹ that has single-crystal data of the modeling compound. 1H NMR spectra were recorded with a DRX-500 NMR spectrometer in deuterated dimethyl sulfoxide ($DMSO-d_6$). The FAB-MS spectra were obtained using JMS-700 HRMS. Elemental analyses were performed with a Heraeus CHN-O-S Rapid-F002 analysis system. UV-vis spectra were measured using a Cary 300 Bio spectrometer. Electrochemical study of the metal complexes dissolved in DMF was performed in a single-compartment, three-electrode cell with a Pt wire counter electrode and a platinum disk working electrode. The reference electrode was Ag/Ag^+ , and the supporting electrolyte was 0.1 M tetrabutylammonium hexafluorophosphate ($TBAPF_6$) in DMF. The square-wave voltammograms (potential step increment: 10 mV; frequency: 25 Hz) were recorded using a potentiostat/galvanostat (PGSTAT 30, Autolab, Eco-Chemie, The Netherlands), and ferrocene was used as a calibration external standard. The thickness of TiO_2 anode was determined by a surface profile meter from Veeco Co. (Dektak 150), USA.

Semiempirical Computation. The DFT calculations were performed to examine the electronic structure of the complexes with the Gaussian 09 program. Ground-state optimization for the three geometric isomers was performed with Becke, three-parameter, Lee-Yang-Parr (B3LYP) exchange-correlations function with DGauss Double-Zeta Valence Polarized (DGDZVP) basis set. The solvent (DMF) effects were included in the calculations using the conductor-like polarizable continuum model (C-PCM). The TD-DFT excited-state calculation of the lowest 60 singlet-singlet electronic transitions for the complexes was performed also at the B3LYP/DGDZVP level³⁵ for the geometry optimization. For computing convenience, the hexylthio-terminal chains in the molecules were modeled by methylthio-substitutions. The overlap weighting factors were set as a default value.³⁶

Device Fabrication and Photovoltaic Characterization. Electrode for the photoanode is $7 \Omega \text{ cm}^{-2}$ fluorine-doped tin oxide (FTO)-coated glass (Merck Glass). The FTO glass was cleaned by detergent, acid, and sonicating in H_2O and then stored in isopropanol before used. A $12 \mu\text{m}$ (particle size: 20 nm) + $4 \mu\text{m}$ (particle size: 400 nm) thick TiO_2 film was deposited on the conducting FTO with screen printer. Detailed methods for TiO_2 film preparation and device

fabrication can be found in our earlier report.³⁷ TiO_2 film was immersed into a $200 \mu\text{M}$ dye solution containing 2–30 mM chenodeoxycholic acid as a coadsorbent in a mixture of DMSO, acetonitrile, and *tert*-butyl alcohol (volume ratio 1:1:1) at room temperature for 12 h. The electrolyte used for the device fabrication contains 0.2 M LiI, 0.03 M I_2 , 0.6 M BMII, 0.1 M GuNCS, and 0.5 M TBP in acetonitrile unless specified otherwise. The photocurrent-voltage characteristics were obtained by applying an external voltage bias to the devices exposed to an irradiance of AM 1.5G (100 mW cm^{-2}) simulated sunlight (Yamashita Denso, Japan) and measuring the generated photocurrent using a Keithley 2400 digital source meter (Keithley, USA). The illuminated active area was 0.25 cm^2 using a metal mask. The dye loading of the DSC was quantified by immersing the practical TiO_2 anodes in a 0.20 mM dye solution, and the concentration difference before and after anode dye loading was quantified by optical spectrophotometry.³⁸

Electrochemical Impedance Spectroscopy. The EIS measurement was performed with an Autolab PG30 potentostat in 50 mV voltage steps with a sinusoidal potential perturbation of 10 mV. The potential perturbation was applied over a frequency range from 1 MHz to 0.1 Hz. The resulting impedance spectra were fitted according to the transmission line model by Bisquert et al. with the ZView software from Scribner.³⁹ The EIS obtained under dark was used to probe TiO_2 /adsorbed dye/electrolyte interphase resistance, which related to the surface coverage of dyed TiO_2 anode.

Transient Absorption Spectroscopy. The TAS measurements were performed in Proteus Ultrafast System with the light path designed by us. A laser light with the wavelength of 470 nm was used to excite the dye molecules in DSC device, and a white light was passed through the device to measure the absorption of the excited dye molecules. The decay of the absorption at 820 nm was used to study the regeneration kinetics of the oxidized dye. The rate constants (or decay time) were extracted by fitting the data using a Surface Explorer software to obtain the rates for the reduction of the oxidized dye by I^- ions in the electrolyte and by charge recombination with the electrons in TiO_2 .⁴⁰

ASSOCIATED CONTENT

Supporting Information

The Supporting Information is available free of charge on the ACS Publications website at DOI: 10.1021/acs.inorgchem.5b01967.

Synthesis of Ligand 29 and CYC-B29, tabulated optical data of the three diastereoisomers CC, TT, and CT, tabulated ground-state vertical excitation data for CC, TT, and CT in DMF, 1H NMR spectra of CC, TT, and CT, illustrated frontier orbitals of CC, TT, and CT, ESI diagrams of devices A, B, and C sensitized with CC, TT, and CT. (PDF)

AUTHOR INFORMATION

Corresponding Author

*E-mail: t610002@cc.ncu.edu.tw.

Notes

The authors declare no competing financial interest.

ACKNOWLEDGMENTS

Financial support from the Ministry of Science and Technology (MOST), Taiwan, ROC (Grant No. NSC 101-2113-M-008-008-MY3), is gratefully acknowledged. The device fabrications and photovoltaic parameter measurements were performed in Advanced Laboratory of Accommodation and Research for Organic Photovoltaics, MOST, Taiwan, ROC.

REFERENCES

- (1) O'Regan, B.; Grätzel, M. *Nature* **1991**, *353*, 737–740.
- (2) Grätzel, M. *Acc. Chem. Res.* **2009**, *42*, 1788–1798.
- (3) Hagfeldt, A.; Boschloo, G.; Sun, L.; Kloo, L.; Pettersson, H. *Chem. Rev.* **2010**, *110*, 6595–6663.
- (4) Grätzel, M. *Inorg. Chem.* **2005**, *44*, 6841–6851.
- (5) Chen, C. Y.; Wang, M.; Li, J. Y.; Pootrakulchote, N.; Alibabaei, L.; Ngoc-le, C. H.; Decoppet, J. D.; Tsai, J. H.; Grätzel, C.; Wu, C. G.; Zakeeruddin, S. M.; Grätzel, M. *ACS Nano* **2009**, *3*, 3103–3109.
- (6) Sauvage, F.; Chen, D.; Comte, P.; Huang, F.; Heiniger, L.-P.; Cheng, Y.-B.; Caruso, R. A.; Grätzel, M. *ACS Nano* **2010**, *4*, 4420–4425.
- (7) Nazeeruddin, M. K.; Kay, A.; Rodicio, L.; Humphry-Baker, R.; Müller, E.; Liska, P.; Vlachopoulos, N.; Grätzel, M. *J. Am. Chem. Soc.* **1993**, *115*, 6382–6390.
- (8) Nguyen, P. T.; Degn, R.; Nguyen, H. T.; Lund, T. *Sol. Energy Mater. Sol. Cells* **2009**, *93*, 1939–1945.
- (9) Asghar, M. I.; Miettunen, K.; Halme, J.; Vahermaa, P.; Toivola, M.; Aitola, K.; Lund, P. *Energy Environ. Sci.* **2010**, *3*, 418–426.
- (10) Islam, A.; Chowdhury, F. A.; Chiba, Y.; Komiyama, R.; Fuke, N.; Ikeda, N.; Nozaki, K.; Han, L. *Chem. Mater.* **2006**, *18*, 5178–5185.
- (11) Funaki, T.; Yanagida, M.; Onozawa-Komatsuzaki, N.; Kasuga, K.; Kawanishi, Y.; Sugihara, H. *Chem. Lett.* **2009**, *38*, 62–63.
- (12) Wadman, S. H.; Kroon, J. M.; Bakker, K.; Lutz, M.; Spek, A. L.; van Klink, G. P. M.; van Koten, G. *Chem. Commun.* **2007**, 1907–1909.
- (13) Wadman, S. H.; Kroon, J. M.; Bakker, K.; Havenith, R. W. A.; van Klink, G. P. M.; van Koten, G. *Organometallics* **2010**, *29*, 1569–1579.
- (14) Wadman, S. H.; Lutz, M.; Tooke, D. M.; Spek, A. L.; Hartl, F.; Havenith, R. W. A.; van Klink, G. P. M.; van Koten, G. *Inorg. Chem.* **2009**, *48*, 1887–1900.
- (15) Bomben, P. G.; Robson, K. C. D.; Sedach, P. A.; Berlinguette, C. P. *Inorg. Chem.* **2009**, *48*, 9631–9643.
- (16) Koivisto, B. D.; Robson, K. C. D.; Berlinguette, C. P. *Inorg. Chem.* **2009**, *48*, 9644–9652.
- (17) Robson, K. C. D.; Koivisto, B. D.; Yella, A.; Spornova, B.; Nazeeruddin, M. K.; Baumgartner, T.; Grätzel, M.; Berlinguette, C. P. *Inorg. Chem.* **2011**, *50*, 5494–5508.
- (18) Bessho, T.; Yoneda, E.; Yum, J.-H.; Guglielmi, M.; Tavernelli, I.; Imai, H.; Rothlisberger, U.; Nazeeruddin, M. K.; Grätzel, M. *J. Am. Chem. Soc.* **2009**, *131*, 5930–5934.
- (19) Wu, K.-L.; Hsu, H.-C.; Chen, K.; Chi, Y.; Chung, M.-W.; Liu, W.-H.; Chou, P.-T. *Chem. Commun.* **2010**, *46*, 5124–5126.
- (20) Bomben, P. G.; Gordon, T. J.; Schott, E.; Berlinguette, C. P. *Angew. Chem., Int. Ed.* **2011**, *50*, 10682–10685.
- (21) Bomben, P. G.; Theriault, K. D.; Berlinguette, C. P. *Eur. J. Inorg. Chem.* **2011**, *2011*, 1806–1814.
- (22) Dragonetti, C.; Valore, A.; Colombo, A.; Roberto, D.; Trifiletti, V.; Manfredi, N.; Salamone, M. M.; Ruffo, R.; Abboto, A. *J. Organomet. Chem.* **2012**, *714*, 88–93.
- (23) Colombo, A.; Dragonetti, C.; Magni, M.; Meroni, D.; Ugo, R.; Marotta, G.; Lobello, M. G.; Salvatori, P.; De Angelis, F. *Dalton Trans.* **2015**, *44*, 11788–11796.
- (24) Dragonetti, C.; Colombo, A.; Magni, M.; Mussini, P.; Nisic, F.; Roberto, D.; Ugo, R.; Valore, A.; Valsecchi, A.; Salvatori, P.; Lobello, M. G.; De Angelis, F. *Inorg. Chem.* **2013**, *52*, 10723–10725.
- (25) Wu, K. L.; Li, C. H.; Chi, Y.; Clifford, J. N.; Cabau, L.; Palomares, E.; Cheng, Y. M.; Pan, H. A.; Chou, P. T. *J. Am. Chem. Soc.* **2012**, *134*, 7488–7496.
- (26) Wu, K. L.; Ku, W. P.; Wang, S. W.; Yella, A.; Chi, Y.; Liu, S. H.; Chou, P. T.; Nazeeruddin, M. K.; Grätzel, M. *Adv. Funct. Mater.* **2013**, *23*, 2285–2294.
- (27) Wang, S.-W.; Wu, K.-L.; Ghadiri, E.; Lobello, M. G.; Ho, S.-T.; Chi, Y.; Moser, J.-E.; De Angelis, F.; Grätzel, M.; Nazeeruddin, M. K. *Chem. Sci.* **2013**, *4*, 2423–2433.
- (28) Wu, K.-L.; Ku, W.-P.; Clifford, J. N.; Palomares, E.; Ho, S.-T.; Chi, Y.; Liu, S.-H.; Chou, P.-T.; Nazeeruddin, M. K.; Grätzel, M. *Energy Environ. Sci.* **2013**, *6*, 859–870.
- (29) Hu, F.-C.; Wang, S.-W.; Chi, Y.; Robertson, N.; Hewat, T.; Hu, Y.; Liu, S.-H.; Chou, P.-T.; Yang, P.-F.; Lin, H.-W. *ChemPhysChem* **2014**, *15*, 1207–1215.
- (30) Chen, C.-Y.; Pootrakulchote, N.; Chen, M.-Y.; Moehl, T.; Tsai, H.-H.; Zakeeruddin, S. M.; Wu, C.-G.; Grätzel, M. *Adv. Energy Mater.* **2012**, *2*, 1503–1509 and unreported data.
- (31) Li, C.; Wu, S.-J.; Wu, C. G. *J. Mater. Chem. A* **2014**, *2*, 17551–17560.
- (32) O'Regan, B.; Walley, K.; Juozapavicius, M.; Anderson, A.; Matar, F.; Ghaddar, T.; Zakeeruddin, S. M.; Klein, C.; Durrant, J. R. *J. Am. Chem. Soc.* **2009**, *131*, 3541–3548.
- (33) Zhang, Z.; Zakeeruddin, S. M.; O'Regan, B.; Humphry-Baker, R.; Grätzel, M. *J. Phys. Chem. B* **2005**, *109*, 21818–21824.
- (34) Reynal, A.; Forneli, A.; Martínez-Ferrero, E.; Sánchez-Díaz, A.; Vidal-Ferran, A.; O'Regan, B.; Palomares, E. *J. Am. Chem. Soc.* **2008**, *130*, 13558–13567.
- (35) Hirata, N.; Lagref, J. J.; Palomares, E. J.; Durrant, J. R.; Nazeeruddin, M. K.; Grätzel, M.; Di Censo, D. D. *Chem. - Eur. J.* **2004**, *10*, 595–602.
- (36) Chen, C. Y.; Lu, H. C.; Wu, C. G.; Chen, J. G.; Ho, K. C. *Adv. Funct. Mater.* **2007**, *17*, 29–36.
- (37) Chen, C. Y.; Chen, J. G.; Wu, S. J.; Li, J. Y.; Wu, C. G.; Ho, K. C. *Angew. Chem., Int. Ed.* **2008**, *47*, 7342–7345.
- (38) Delley, B. *J. Chem. Phys.* **2000**, *113*, 7756–7764.
- (39) Fabregat-Santiago, F.; Garcia-Belmonte, G.; Bisquert, J.; Zaban, A.; Salvador, P. *J. Phys. Chem. B* **2002**, *106*, 334–339.
- (40) Mozer, A. J.; Panda, D. K.; Gambhir, S.; Winther-Jensen, B.; Wallace, G. G. *J. Am. Chem. Soc.* **2010**, *132*, 9543–9545.